Journal of the European Ceramic Society 43 (2023) 6967–6973

Contents lists available at ScienceDirect

Journal of the European Ceramic Society

journal homepage: www.elsevier.com/locate/jeurceramsoc

Induced p-type semiconductivity in Mg-doped $Nd_2Zr_2O_7$ pyrochlore system

X. Vendrell [a,b,*], E.L. Santos-Veiga [c], H. Beltrán-Mir [c], E. Cordoncillo [c], L. Mestres [a,b]

[a] Department of Inorganic and Organic Chemistry, Universitat de Barcelona, 08028 Barcelona, Spain
[b] Institute of Nanoscience & Nanotechnology, Universitat de Barcelona, 08028 Barcelona, Spain
[c] Department of Inorganic and Organic Chemistry, Universitat Jaume I, 12071 Castelló, Spain

ARTICLE INFO

Keywords:
Pyrochlore
Doping
Oxygen vacancies
Ionic conductivity
P-type semiconductivity

ABSTRACT

Heterovalent B-site MgO substitution in the $Nd_2Zr_2O_7$-system ($Nd_2Zr_{2-x}Mg_xO_{7-x}$) has been explored. The pyrochlores were synthesized by a polymeric sol-gel method and characterized by X-ray diffraction (XRD), Raman spectroscopy and Scanning Electron Microscopy to determine structure, phase composition and microstructure. Impedance Spectroscopy (IS) was employed to study the electrical behavior of the ceramics over the ranges 200–800 °C and under pure N_2 and O_2. The XRD showed that the solid solution limit was $x > 0.02$ and all the materials show a cubic $Fd\bar{3}m$ structure. The Raman results confirm the structural disorder created by the introduction of Mg^{2+} and the subsequent generation of oxygen vacancies. The IS data shows a dramatical increase of the oxide-ion conductivity when doping and that the conductivity depends strongly on the atmosphere, leading to p-type semiconductivity under pure O_2 atmosphere. The present study highlights the use of heterovalent dopants to drastically increase the oxide-ion conductivity of pyrochlore-like materials.

1. Introduction

Pyrochlore-based materials ($A_2B_2O_7$) show a vast variety of physical and chemical properties and, therefore, in the last decades, pyrochlores have attracted much attention due to their wide range of applications such as in the production of clean energy in solid-oxide fuel cells [1,2], in catalysis to recycle CO_2 [3,4] or oxidize CO [5], as thermal barriers coatings [6] or to immobilize nuclear waste [7].

The properties of the pyrochlore-based materials rely on the high physical and chemical flexibility of the cubic, $Fd\bar{3}m$, structure. The ideal fully ordered pyrochlore structure can be considered as a superstructure of the ideal fluorite structure ($Fm\bar{3}m$) and the general formula is commonly described as $A_2B_2O_6O'$, where the A and B cations occupy the Wyckoff positions of 16d (1/2, 1/2, 1/2) and 16c (0, 0, 0) site, respectively. The O and O' oxygen anions are in the 48 f (x, 1/8, 1/8) and 8b (3/8, 3/8, 3/8) sites, respectively and the 8a (1/8, 1/8, 1/8) oxygen site O'' in a pyrochlore will be vacant, which leads to enhanced oxide-ion mobility. Usually, A-site cations are tri-valent rare-earth located within a distorted cube and coordinated with six O anions and two O' anions, while the B site being 3d, 4d, and 5d transition element with suitable oxidation state to satisfy charge balance and is surrounded by two 8a inherent oxygen vacancies and coordinated with six O anions [8]. The properties of pyrochlore materials strongly depend on the r_A/r_B ratio [9] and the ordered cubic phase only exists when $1.46 \leq r_A/r_B \leq 1.78$. Generally, when the A and B cations are fully ordered the oxygen conductivity is rather low, however, by substituting different cations in A and/or B sites, the degree of disorder can be adjusted to increase the oxide-ion conductivity [10]. The large A and B cation substitutions can satisfy the radius ration condition to obtain a neutral and chemically stable pyrochlore structure. Therefore, the addition A and B-site cations may deviate the system to a complete disordered structure leading to an enhanced oxide-ion conductivity. Moreover, the presence of cationic disorder leads to the formation of Frenkel defects [11], which can enhance the diffusivity of oxide-ions and, therefore, increase the ionic conductivity.

The RE_2O_3-ZrO_2-system (RE: rare earth) has been explored in many applications due to its high temperature stability, good corrosion resistance and in the facility to immobilize Pu for nuclear applications [12,13]. In addition, the RE_2O_3-ZrO_2-system has also been, recently, explored as potential ionic conductors [14–17]. In this sense, the Nd_2O_3-ZrO_2-system has been explored as ionic conductor showing similar oxide-ion conductivity to the Y-doped ZrO_2 fluorite-like system [18–21]. Although the ordering-disordering relation by varying the stoichiometry-non-stoichiometry of the local structure of the A- and B-site cations in the $Nd_2Zr_2O_7$-system [14] has been explored as potential oxide-ion conductors with remarkable results, it is well known

* Corresponding author at: Department of Inorganic and Organic Chemistry, Universitat de Barcelona, 08028 Barcelona, Spain.
E-mail address: xavier.vendrell@ub.edu (X. Vendrell).

https://doi.org/10.1016/j.jeurceramsoc.2023.07.061
Received 4 May 2023; Received in revised form 9 July 2023; Accepted 26 July 2023
Available online 27 July 2023

that maintaining the nominal compositions while the synthesis and sintering temperatures are far above 1000 °C is quite challenging, we propose to explore the doping engineering in order to increase the oxygen vacancies in the $Nd_2Zr_2O_7$-system by substituting Zr^{4+} by Mg^{2+}.

2. Experimental section

Five compositions based on the general formula $Nd_2Zr_{2-x}Mg_xO_{7-x}$, with x = 0.0, 0.005, 0.01, 0.02 and 0.04, labeled NZO, NZOMg05, NZOMg1, NZOMg2 and NZOMg4, respectively, were prepared by a polymeric sol-gel procedure using Nd_2O_3 (99.9%, Sigma-Aldrich), $ZrOCl_2{\cdot}8\,H_2O$ (99%, Fluka) and $Mg(NO_3)_2$ (99%, Sigma-Aldrich) as precursors. The required amount of Nd_2O_3 was dissolved with nitric acid 13 M and the necessary amount of $ZrOCl_2{\cdot}8\,H_2O$ was solved in 50 mL of water and stirred until complete dissolution. The two homogenous solutions were then mixed and the necessary amounts of citric acid (99.5%, Sigma-Aldrich) and 0.5 mL of polyethylene glycol were added as quelating and polymerizing agents. If necessary, the dopant agent, $Mg(NO_3)_2$, was added and the final solution was stirred and heated at 70 °C for 12 h. A transparent gel formed was dried at 100 °C in an oven for approximately 1 day. Finally, the dry gel was ground with an agate mortar and pestle, decomposed at 5 °C min^{-1} to 800 °C for 5 h. Powder samples were cooled, crushed, and sieved through a 0.9 μm mesh sieve and pressed into pellets of 6 mm diameter at 700 MPa of uniaxial pressing. Pellets were sintered at 1500 °C for 10 h with a heating and cooling rate of 2 °C min^{-1}. The thermal treatments were carried out under air atmosphere using a tubular high temperature furnace controlled with an Eurotherm 2416 controller. Pellet densities for all compositions were ~ 93%.

The phase(s) present were analyzed by powder X-ray diffraction (XRD) using a PANalytical X'Pert PRO MPD Alpha 1, with Cu Kα radiation. Data were collected by step scanning from 2Θ = 4–80° with a step size of 0.017° and 50 s counting time at each step. The cubic lattice parameter was determined by a LeBail fitting procedure as implemented in the Fullprof suite [22]. The Raman scattering spectra were obtained on a Jobin-Yvon Labram HR 800 (Horiba) spectrometer with an Ar excitation wavelength of 532 nm. Microstructure was evaluated using a scanning electron microscope (SEM), JEOL J-6510, equipped with a spectrometer for energy-dispersion analysis of X-rays (EDX). The average grain size was determined from the SEM images using an image processing and analysis software (ImageJ). The grain size was expressed as Feret's diameter using more than 300 grains in each measurement.

For electrical property measurements, gold electrodes were sputtered on opposite pellet faces. Samples with electrodes were placed in a conductivity jig with two-electrode configuration in an in-house furnace which allows to control the atmosphere of the chamber. Measurements were made with an impedance analyser, HP4192A, in the frequency range 5 Hz-3 MHz, the nominal *ac* voltage used was 100 mV and no *dc* voltage was applied during the impedance measurements. Samples were analysed under dried atmospheres of O_2 and N_2 from room temperature to 800 °C. At each temperature, the system was allowed to equilibrate for 1 h, prior to impedance measurements. Impedance data were corrected for sample geometry and electrode contact area; this allowed resistance and capacitance to be reported in resistivity and permittivity units of Ω cm and F cm^{-1}, respectively. Open circuit measurements of an empty jig were used to obtain the blank parallel capacitance, C_0, of the jig and leads, which was subtracted from the values obtained with a sample present in the jig. In order to obtain the C_0 value, the jig was assembled with electrodes of similar dimension, but without a sample in place. Closed circuit measurements were obtained by connecting the two electrodes directly and used to correct for the series jig resistance. Corrected data were analysed and modelled using Zview (Scriber Associates Inc.) software. Details of the impedance analysis can be found extendedly in the literature [23–27].

3. Results & discussion

Pellets sintered at 1500 °C for 10 h were ground and analysed by XRD. Samples with no dopant added or with low amounts of dopant up to x = 0.02 appeared to be single phase. Due to the structural similarity between the fluorite and pyrochlore structures it is difficult to assign one or other structure. Although, the fluorite phase is commonly observed when ceramics are prepared at low temperatures and transforms to the pyrochlore structure when annealed at temperatures higher than 1100–1200 °C [28–30]. However, the presence of super-lattice peaks at 2Θ ≈ 14° (111), and 37° (331) are considered as the fingerprint of pyrochlore crystal structure and used to differentiate from the fluorite structure. As shown in Fig. 1(a) all the peaks belonging to the pyrochlore structure are present and, therefore, the neodymium zirconium oxide formed belongs to the ordered pyrochlore structure (PDF#00–017–0458).

When ceramics are doped with larger amounts of Mg^{2+}, x = 0.04, extra tiny peaks are observed at 30° < 2Θ< 32°, which can be assigned to hexagonal Nd_2O_3 (PDF#01–075–2255), Fig. 1(b) inset. The presence of such peaks denotes that the solubility of Mg^{2+} into the NZO structure is limited to x = 0.02, however as pointed out by J-Y Ma et al. [13] an incomplete reaction of raw materials cannot be discarded. XRD patterns of all the prepared ceramics were indexed and refined using a cubic unit cell, space group $Fd\bar{3}m$ as expected for NZO-based ceramics, Fig. S1. The evolution of the lattice parameter as a function of Mg^{2+} amount is shown in Fig. 1(c). For low content of magnesium, x ≤ 0.02, and despite that the ionic radii of Zr^{4+} and Mg^{2+} are both 0.72 Å in a 6-fold coordination [31], the lattice parameters slightly increase with respect to pure NZO, which suggest that the addition of Mg^{2+} generates oxygen vacancies and therefore, an expansion of the lattice. It is worth mentioning that the cell parameters do not follow the Vegard's law, which could be in agreement with the formation of oxygen vacancies [32]. Moreover, a small displacement towards lower 2θ angles of the Bragg peaks with respect to the NZO sample is also observed in the XRD patterns for compositions x ≤ 0.01. According to the Bragg`s Law, nλ= 2dsenθ, where d is the interplanar distance, θ is the Bragg angle and λ is diffraction wavelength, an expansion of the lattice produces an increase of the interplanar distance and therefore a decrease of the 2θ angle. This behaviour together with the absence of secondary phases indicate that Mg^{2+} has diffused into the NZO lattice to form a solid solution. However, at higher content of dopant, x ≥ 0.02 the cell parameter is practically invariable, which agrees with the presence of unreacted Nd_2O_3 and confirming that the solubility limit is at x = 0.02. Additionally, the XRD patterns of the samples calcined at 800 °C for 5 h are shown in Fig S2.

Raman spectroscopy technique can be used to provide an unequivocal information to distinguish between the ordered pyrochlore structure from the fluorite structure. Moreover, it can also be used to highlight the details of metal-oxygen vibrations at the atomic scale [33]. Therefore, all the sintered ceramics were analysed by Raman spectroscopy over the frequency range 150–800 cm^{-1}. Based on group's theory, the cubic pyrochlore, $A_2B_2O_7$ shows typically 6 active Raman modes which can be distributed as $A_{1\,g}+E_g+4\,F_{2\,g}$ [34,35]. However, the cubic undistorted-fluorite structure has only one Raman active mode $T_{2\,g}$ [36]. As shown in Fig. 2, the Raman spectra of the NZO and Mg-doped NZO ceramics present the typical vibrations corresponding to the pyrochlore phase with bands appearing at approximately, 300, 400, 500, 520 and 630 cm^{-1}. Similar spectra were observed by Mandal et al. [37,38] when analysing Y or Gd-doped NZO. However, in their analysis of the Raman spectra of NZO-based pyrochlores, there was little evidence of bands appearing in the frequency range 600–700 cm^{-1} which are observed in our case. This could be attributed to the different synthesis routes and sintering temperatures employed [13,28,39] which have shown to have a great impact on the microstructure and on the Raman spectra. Moreover, such bands may appear as a broad and undefined band shifted depending on the pyrochlore composition[14,34].

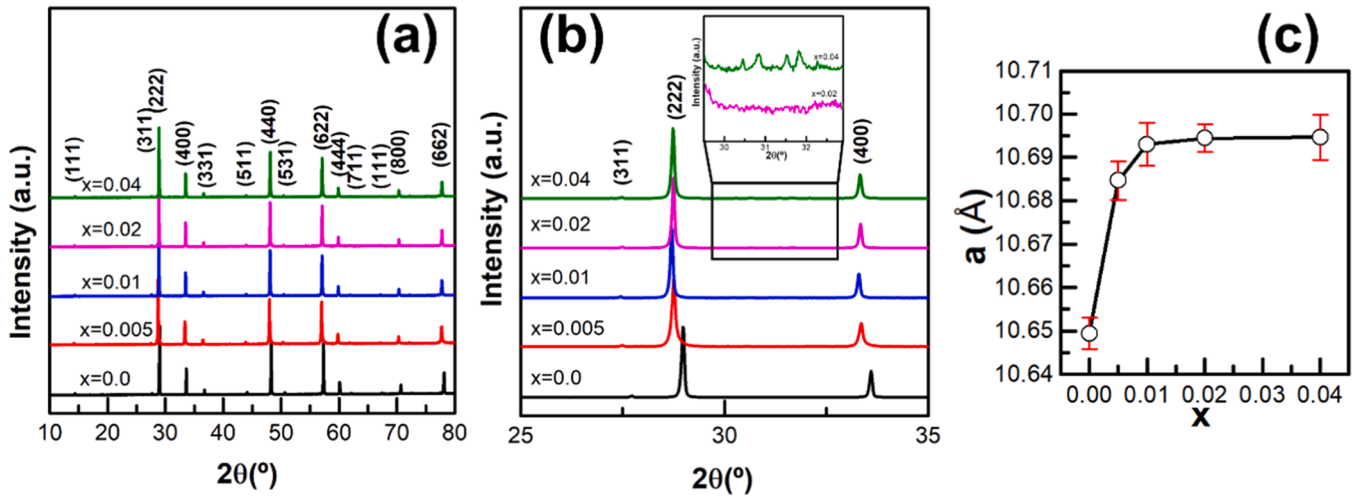

Fig. 1. (a) X-ray diffraction (XRD) patterns for the $Nd_2Zr_{2-x}Mg_xO_{7-x}$ (x = 0.0, 0.005, 0.01, 0.02 and 0.04) of powders calcined at 800 °C for 5 h and sintered at 1500 °C for 10 h. (b) The (311), (222) and (400) diffraction peaks of the pyrochlore phase for all compositions. (c) Evolution of the a parameter as a function of x.

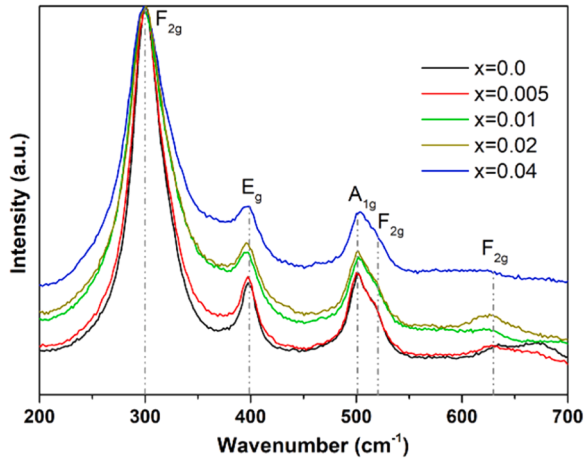

Fig. 2. Raman spectra of the $Nd_2Zr_{2-x}Mg_xO_{7-x}$ (x = 0.0, 0.005, 0.01, 0.02 and 0.04) samples sintered at 1500 °C for 10 h.

According to the literature the Raman bands observed at higher frequencies are all principally B-O stretching modes, while the lower frequency region includes coupled B-O stretches, O-B-O bends, and A-O stretches [40]. Therefore, in agreement with previous Raman measurements reported in the literature [14,29,34,38,41,42], the Raman band observed at around 300 cm^{-1} is assigned to the $F_{2\,g}$ mode and is primarily attributed to the B-O-B bending vibrations. The bands occurring around 400 and 500 cm^{-1} are commonly attributed to B-O stretching and B-O-B bending vibrations mixed with A-O and B-O stretch, respectively, and are assigned to E_g and $A_{1\,g}$ modes. At slightly higher frequencies, 520 cm^{-1} approximately the $F_{2\,g}$ mode is observed corresponding to a B-O-B bending vibration. Finally, the broad bands appearing in the frequency range 600–700 cm^{-1}, whose intensity depend on the Mg content, can be attributed to B-O stretching vibrations and assigned to a $F_{2\,g}$ mode. As clearly shown in Fig. 2, no significant shifts of the main bands are observed when increasing the content of Mg, however, as the content of Mg increases a large broadening of the Raman bands is obtained. The band broadening could be partially attributed to the decrease of the particle size, as seen in the micrographs, Fig. 3, where a decrease from ~1 μm for pure NZO to ~0.25 μm for NZOMg1. However, all the samples are in micro regime as the XRD patterns are reasonably sharp and no broadening is observed. Therefore, the Raman broadening can be attributed to an increase of disorder due to A-site doping and also due to the presence of vacancy defects that disrupt the translational symmetry in the lattice and relaxes de k ≈ 0 selection rule [37]. Since all the Raman active vibrations include oxygen motion (stretching and bending vibrations) the origin of broadening is primarily due to the structural disorder created by the existence of oxygen vacancies and by the introduction of Mg^{2+}. Moreover, the intensity of the 600–700 cm^{-1} bands attributed to B-O stretching vibration modes changes as the content of Mg increases. The weakening of intensity of the 600–700 cm^{-1} bands (which are related to 48 f oxygen) indicates that the disorder is associated with 48 f oxygen site [7,43]. On the other side, the 8b oxygen remain unalterable, as the intensity of the 400 cm^{-1} band does not vary significantly when doping with Mg.

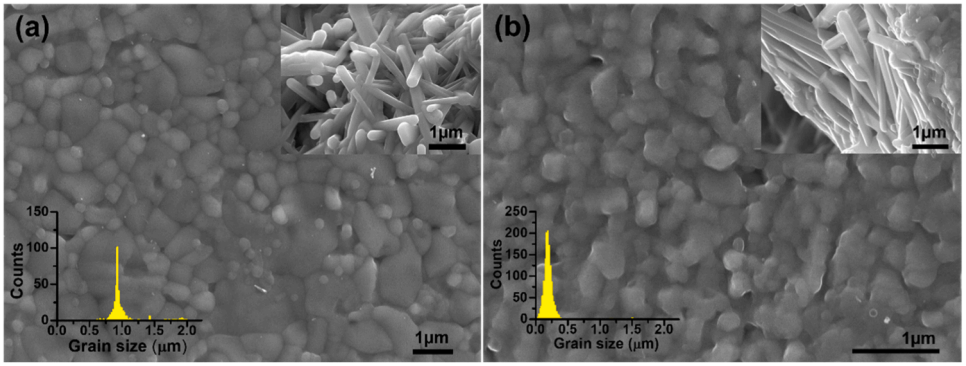

Fig. 3. Micrographs of the (a) $Nd_2Zr_2O_7$ and (b) $Nd_2Zr_{2-x}Mg_xO_{7-x}$ (x = 0.01) samples. The inset show the grain size distribution of each sample.

The microstructure of pure NZO and NZOMg1 ceramics are revealed by thermal etching on polished samples at 1350 °C for 5 min. As shown in Fig. 3(a) pure NZO presents a bimodal microstructure with grains ranging from about 500 nm to a few micrometres, with an average grain size of ~0.97 ± 0.46 μm. The micrograph and the grain distributions of pure NZO also show the presence of some large grains with undefined form, however, when doping with Mg^{2+} ceramics show a drastic decrease of the grain size together with an increase of the grain size distribution uniformity, Fig. 3(b). The average grain size of the NZOMg1 ceramic is ~0.22 ± 0.18 μm. The insets of Fig. 3(a) & (b) show the fracture surface of NZO and NZOMg1 which reveals the presence of enlarged grains. Contrary to what observed by J-Y Ma et al. [13] the EDS analysis (not shown) do not show the presence of two different phases or an inhomogeneous distribution of MgO in the $Nd_2Zr_2O_7$ structure, indicating that the preparation method used promotes the formation of a solid solution.

A typical set of impedance data, recorded in dry N_2 at 600 °C and presented in different formats, are shown in Fig. 4 for a NZOMg1 pellet. Similar response was observed for all Mg-doped compositions. The impedance complex plots, Z * , (a) shows a semi-circular arc at high frequencies and evidences of a smaller partial semi-circular arc at low frequencies. The Z''/M'' spectroscopic plots at 600 °C (b) clearly show a single Debye peak in each spectrum with approximately similar peak maximum frequencies. The peak maximum of an ideal Debye-like M'' peak is inversely proportional to the capacitance of an RC element responsible for the peak. Therefore, since the smallest capacitance usually represents the bulk component, the M'' peak and the associated Z'' peak, enable the assignment of these peaks to the bulk sample conductivity. Thus, at low temperatures, samples can be represented by a single RC element in which the total resistance, R, corresponds to the resistance of the bulk and the capacitance, C, represents the bulk capacitance of the samples.

At 700 °C, Z * plots confirm the presence of a large semi-circular arc, the appearance of a second semi-circular arc at lower frequencies and an inclined spike with some curvature at the lowest frequencies (c). The logC'/logf plots (Fig. 4(d)) for the same data at 700 °C show evidences of a frequency-independent plateau at high frequencies with values ~5 pF cm^{-1}, which can be attributed to the sample bulk. The C′ values increase with decreasing frequency, with a poorly resolved plateau at ~180 pF cm^{-1}, which represents the grain boundary capacitance. At lower frequencies, the capacitance rises quickly to 0.01 μF cm^{-1} at 5 Hz; this value is typical of ion blocking at sample-electrode interface and the formation of a double-layer capacitance. Moreover, the inclined spike shown in Fig. 4(c) at low frequencies is attributed to the diffusion of oxygen molecules toward and away from sample-electrode interface, and therefore, attributed to a Warburg impedance. Consequently, we associate the low-frequency impedance data to primarily oxide-ion conduction. Similar behaviour was observed for all samples.

The total resistivity of all the samples, at different temperatures, was obtained from the intercepts on the real Z′ axis extracted from the Z * plots. Fig. 5(a) shows the Z * plots of all samples at 700 °C. The effect of doping is evident, samples resistance decreases drastically. This effect can also be seen in the Arrhenius plots shown in Fig. 5(b) and (c). The introduction of Mg^{2+} in the NZO pyrochlore structure promotes the oxide-ion conductivity by increasing the conductivity from 6.48 × 10^{-6} S cm^{-1} to 2.47 × 10^{-4} S cm^{-1} for un-doped NZO and NZOMg1 samples, respectively at 800 °C. The conductivity values obtained once doping are similar to other pyrochlore systems reported in the literature, such as

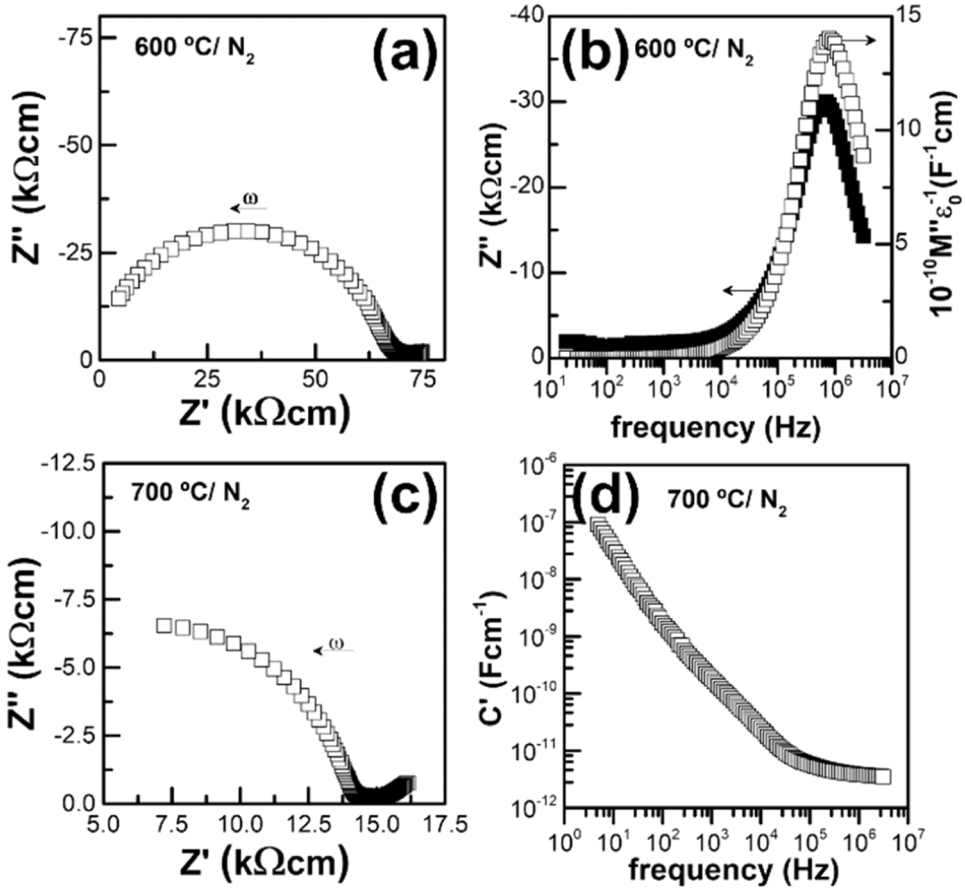

Fig. 4. (a) Impedance complex plane plots, Z * , at 600 °C for $Nd_2Zr_2O_7$ under dry N_2 atmosphere. (b) Z''/M'' spectroscopic plots for $Nd_2Zr_2O_7$. (c) Impedance complex plane plots, Z * , at 700 °C for $Nd_2Zr_{2-x}Mg_xO_{7-x}$ (x = 0.01) under dry N_2 atmosphere. (d) C′/log f spectroscopic plot recorded in dry N_2 at 700 °C for $Nd_2Zr_{2-x}Mg_xO_{7-x}$ (x = 0.01).

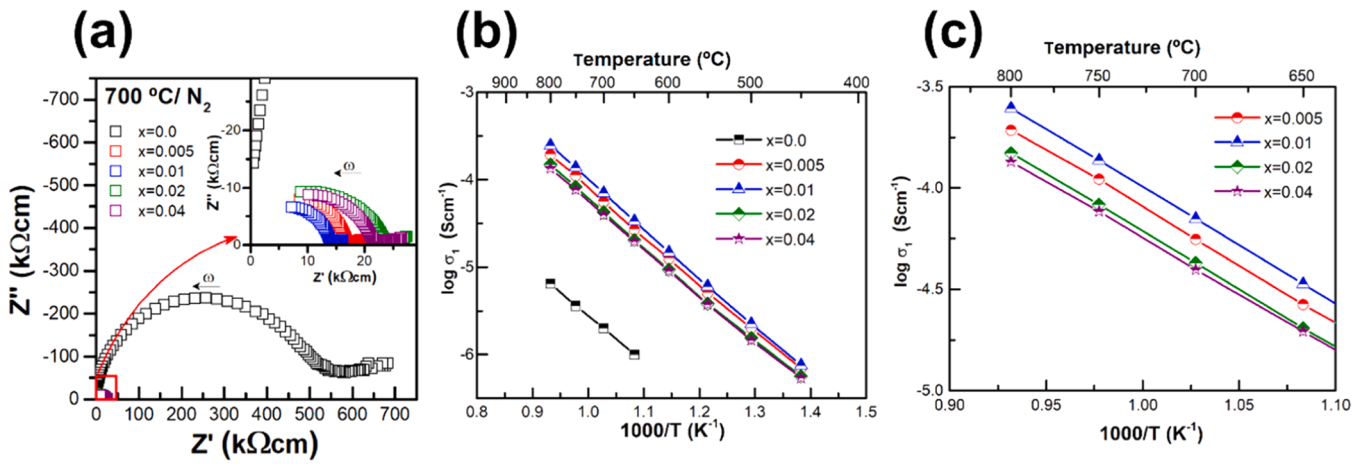

Fig. 5. (a) Impedance complex plane plots, Z * , at 700 °C under dry N_2 atmosphere, (b) Arrhenius plot of bulk (σ_1) and (c) detail of the Arrhenius plot of bulk (σ_1) for $Nd_2Zr_2O_7$ and $Nd_2Zr_{2-x}Mg_xO_{7-x}$ (x = 0.0, 0.005, 0.01, 0.02 and 0.04).

$Sm_2Zr_2O_7$ [44], $Gd_2Zr_2O_7$ [45], Pr_2Zr_2O7 [46], Y_2TiO_7 [47] or Er_2MnTiO_7 [48]-based systems. The activation energies and the pre-exponential factors of all samples, extracted from the Arrhenius plots in Fig. 5(b), are shown in Table 1. There is no significant variation of the activation energies as a function of the dopant content, therefore, the conduction mechanism remains the same in all cases, oxygen-ion conduction. However, a significant increase of the preexponential factor value is observed when doping, reaching a maximum for the NZOMg1 sample, which also shows the maximum conductivity. It is well-know that the preexponential factor is related with the density of the mobile charge carriers, therefore, NZOMg1 has a much higher concentration of mobile charge carriers than the other samples.

Commonly, oxide-ion-conductors show an increase of electronic conductivity a low oxygen partial pressures, by the onset of n-type electronic conduction. However, little information is available on the other side, at high pO_2, where in it is assumed that the uptake of oxygen may occur by a mechanism shown in Eq. 1 using the Kroger-Vink notation

$$V_0^{\bullet\bullet} + \frac{1}{2}O_2 \rightarrow O_0^x + 2h^{\bullet} \quad (1)$$

The location of the holes responsible for conductivity was traditionally attributed to impurities such as Fe^{3+} which could ionise to Fe^{4+} [49]. The location is now believed to be on lattice oxide ions, in part because high purity chemicals were used for the syntheses, and because the other cations in the structure are already in their highest valence states and cannot be considered as a possible location for the holes.

It has, recently, been demonstrated that p-type electronic conduction is introduced in yttria-stabilized zirconia (YSZ) [17,50–52] in oxygen pyrochlore-type structures [46] or on acceptor-doped $BaTiO_3$ [53,54] at high pO_2, by applying a small *dc* bias or by the combination of both. Therefore, in order to get further information of the conduction mechanism of the samples, impedance measurements were performed under different atmosphere conditions. Samples were analysed under dry N_2 and dry O_2 at different temperatures. The data shown in Fig. 6 indicates in both samples, NZO (a & b) and NZOMg1 (c & d) the presence of p-type conduction under O_2 atmosphere (1 atm). As it can be seen, several effects are observed: first, the bulk or the total resistance of the sample decreases, Fig. 6(a) and (c); and second, the Warburg spike contracts greatly, Fig. 6(c) inset. The later can only be observed in (c) because the Warburg spike is not observed in (a) at the studied temperature. This effect is completely reversible and when the atmosphere was changed from dry O_2 (1 atm) to dry N_2 (1 atm), the conductivity recovered its original values after a few minutes.

The increase of the conductivity can be explained in terms of the absorption of oxygen on the surface, and therefore, boosting the number of holes. As described in Eq. 1, holes are located on oxygen, creating O^- species, which can participate in the following equilibria (Eq. 2)

$$O_2(g) \rightleftharpoons O_2(ads) \rightleftharpoons O_2^- \rightleftharpoons O_2^{2-} / 2O^- \rightleftharpoons 2O^{2-}(surface) \rightleftharpoons 2O^{2-}(bulk) \quad (2)$$

The contraction of the Warburg spike is also shown in the capacitance data, Fig. 6(d). The low-frequency capacitance values decrease when switching to O_2 atmosphere, which confirms that is no longer associated with the charge transfer mechanism occurring at the interface. This process can, also, be attributed to the creation of a parallel electronic conduction mechanism [52].

The sensitivity of the samples resistance to changes in pO_2 is direct evidence that the electronic conductivity mechanism is p-type. Commonly, in the literature, the p-type conductivity has been attributed, but rarely proven, to unavoidable impurities such as Fe. However, recent results on doped barium titanate perovskites indicate that the underbonded oxide ions could be the source and the location of holes [53,54]. This behaviour has also been observed recently in oxide-ion conductors such as YSZ-based [17,50,51] and pyrochlore-based [46] materials.

Table 1
Activation energies and pre-exponential factor extracted from the Arrhenius plots $Nd_2Zr_2O_7$ and $Nd_2Zr_{2-x}Mg_xO_{7-x}$ (x = 0.0, 0.005, 0.01, 0.02 and 0.04) samples.

x	Ea (eV)	σ_0 (S cm^{-1} K^{-1})
0,0	1,06 (6)	$1{,}38{\cdot}10^3$ (0,68)
0005	1,04 (3)	$5{,}04{\cdot}10^4$ (0,91)
0,01	1,09 (5)	$9{,}15{\cdot}10^4$ (0,42)
0,02	1,06 (8)	$2{,}87{\cdot}10^4$ (1,02)
0,04	1,04 (6)	$2{,}80{\cdot}10^4$ (0,96)

4. Conclusions

$Nd_2Zr_{2-x}Mg_xO_{7-x}$, with x = 0.0, 0.005, 0.01, 0.02 and 0.04 pyrochlore materials have been prepared by a coprecipitation method. The special care of the reagents and the synthesis procedure assures the formation of a single phase up to x = 0.02 of dopant, at higher amounts of Mg^{2+} tiny peaks of hexagonal Nd_2O_3 are observed. The XRD patterns of all samples confirm the presence of super-lattice peaks, which agrees with the formation of the pyrochlore crystal structure. Raman spectroscopy not only confirms the formation of the pyrochlore structure, but also an increase of disorder due to the presence of vacancy defects oxygen promoted by the introduction of Mg^{2+}. As expected, the addition of MgO as dopant inhibits the grain growth and the formation of

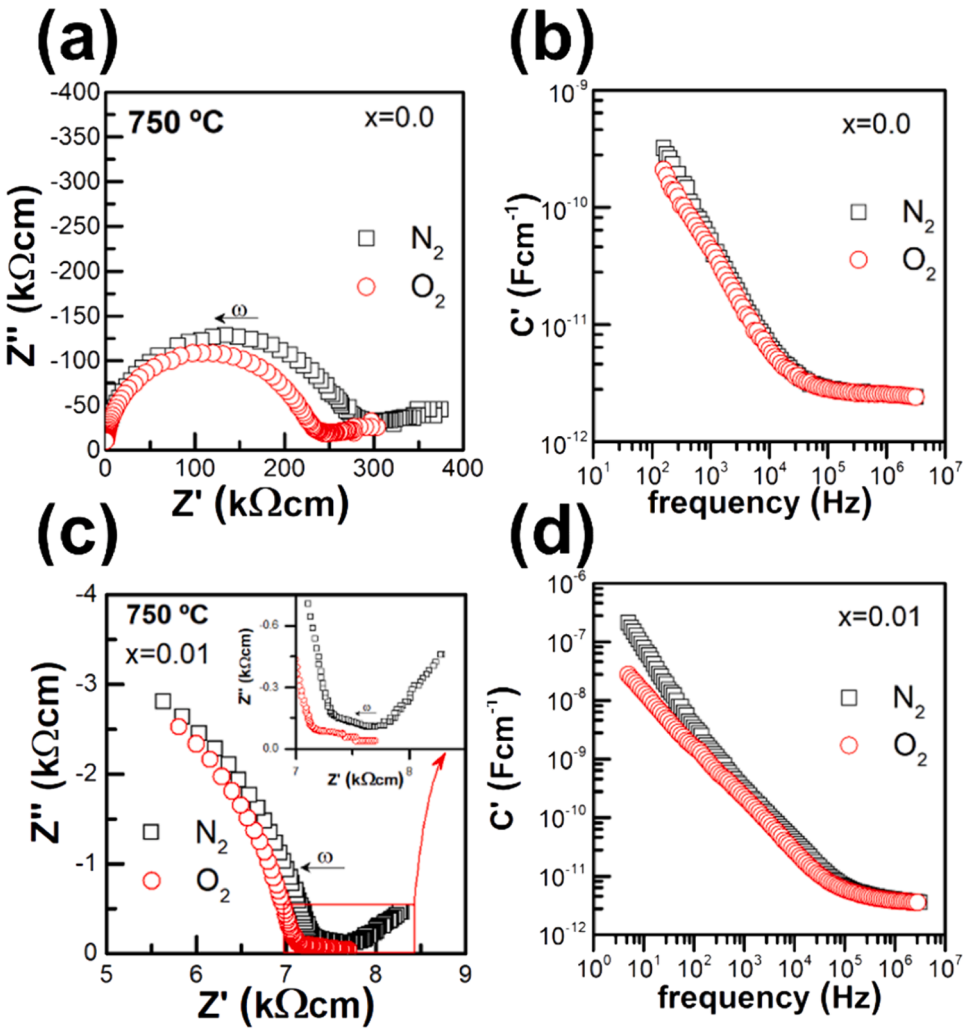

Fig. 6. Impedance complex plane plots, Z * , at 750 °C under dry N_2 and O_2 for (a) $Nd_2Zr_2O_7$ and for (c) $Nd_2Zr_{2-x}Mg_xO_{7-x}$ (x = 0.01). C′/log f spectroscopic plot for (b) $Nd_2Zr_2O_7$ and for (d) $Nd_2Zr_{2-x}Mg_xO_{7-x}$ (x = 0.01) at 750 °C under dry N_2 and O_2.

enlarged grains.

The electrical characterization of the NZO-based ceramics by impedance spectroscopy confirms that all the prepared ceramics are electrically homogeneous at all the interval of temperatures studied. Doping with MgO increases drastically the oxide-ion conductivity of the NZO-pyrochlore under N_2 atmosphere. When switching from pure N_2 atmosphere to pure O_2 atmosphere samples become mixed conductors due to the introduction of p-type semiconductivity, where holes are assumed to be located in underbonded oxide ions.

This results, on the one hand, confirms that the onset of p-type conductivity in oxide-ion conductors; and on the other hand, reinforces the possibilities to explore pyrochlore structures as oxide-ion conductors in fuel cells applications.

Declaration of Competing Interest

The authors declare that they have no known competing financial interests or personal relationships that could have appeared to influence the work reported in this paper.

Acknowledgments

X.V. is a Serra Húnter Lecturer fellow and is grateful to the Generalitat de Catalunya. X. V. and L. M. acknowledge the financial support from the Spanish Ministerio de Ciencia e Innovación (PID2020–116031RB-I00). H.B-M, E.C. and E.L.S.V. thank the Spanish Ministerio de Ciencia e Innovación (PID2020–116149GB-I00) for the financial support. E.L.S.V thanks the Generalitat Valenciana (GRISOLIA/2019/054) for the predoctoral contract.

Appendix A. Supporting information

Supplementary data associated with this article can be found in the online version at doi:10.1016/j.jeurceramsoc.2023.07.061.

References

[1] R.S. Rejith, S. Solomon, Influence of pyrochlore domains on the structure and electrical properties $Gd_{2-x}Dy_xZr_{1.5}Hf_{0.5}O_7$ energy materials, J. Alloy. Compd. 855 (2021), 157291.

[2] F. Zhong, S. Yang, C. Chen, H. Fang, K. Chen, C. Zhou, L. Lin, Y. Luo, C. Au, L. Jiang, Defect-induced pyrochlore $Pr_2Zr_2O_7$ cathode rich in oxygen vacancies for direct ammonia solid oxide fuel cells, J. Power Sources 520 (2022), 230847.

[3] J. Bai, Y. Fu, W. Kong, B. Pan, C. Yuan, S. Li, J. Wang, J. Zhang, Y. Sun, Design of Ni-substituted $La_2(CeZrNi)_2O_7$ pyrochlore catalysts for methane dry reforming, ChemNanoMat 8 (2022).

[4] E. le Saché, L. Pastor-Pérez, D. Watson, A. Sepúlveda-Escribano, T.R. Reina, Ni stabilised on inorganic complex structures: superior catalysts for chemical CO_2 recycling via dry reforming of methane, Appl. Catal. B Environ. 236 (2018) 458–465.

[5] E.L. dos Santos Veiga, X.V. Villafruela, J. Llorca, H. Beltrán-Mir, E. Cordoncillo, The catalytic activity of the $Pr_2Zr_{2-x}Fe_xO_{7\pm\delta}$ system for the CO oxidation reaction, J. Am. Ceram. Soc. 106 (2022) 1369–1380.

[6] X. Wang, L. Guo, H. Zhang, S. Gong, H. Guo, Structural evolution and thermal conductivities of $(Gd_{1-x}Yb_x)_2Zr_2O_7$ (x=0, 0.02, 0.04, 0.06, 0.08, 0.1) ceramics for thermal barrier coatings, Ceram. Int. 41 (2015) 12621–12625.

[7] C. Nandi, A.K. Poswal, M. Jafar, S. Kesari, V. Grover, R. Rao, A. Prakash, P. G. Behere, Effect of Ce^{4+}-substitution at A and B sites of $Nd_2Zr_2O_7$: a study for plutonium incorporation in pyrochlores, J. Nucl. Mater. 539 (2020), 152342.

[8] M.A. Subramanian, G. Aravamudan, G.V. Subba, Rao, Oxide pyrochlores — A review, Prog. Solid State Chem. 15 (1983) 55–143.

[9] A. Fernandes, D. McKay, S. Sneddon, D.M. Dawson, S. Lawson, R. Veazey, K. R. Whittle, S.E. Ashbrook, Phase composition and disorder in $La_2(Sn,Ti)_2O_7$ ceramics: New insights from NMR crystallography, J. Phys. Chem. C. 120 (2016) 20288–20296.

[10] S. Kramer, M. Spears, H.L. Tuller, Conduction in titanate pyrochlores: role of dopants, Solid State Ion. 72 (1994) 59–66.

[11] J.A. Díaz-Guillén, M.R. Díaz-Guillén, K.P. Padmasree, A.F. Fuentes, J. Santamaría, C. León, High ionic conductivity in the pyrochlore-type $Gd_{2-y}La_yZr_2O_7$ solid solution ($0 \leq y \leq 1$), Solid State Ion. 179 (2008) 2160–2164.

[12] R.C. Ewing, W.J. Weber, J. Lian, Nuclear waste disposal—pyrochlore ($A_2B_2O_7$): nuclear waste form for the immobilization of plutonium and "minor" actinides, J. Appl. Phys. 95 (2004) 5949–5971.

[13] J.-Y. Ma, Y.-B. Zhang, J.-X. Wang, Y.-Y. Song, T. Zhou, Y. Wang, H.-Y. Wang, J. Wang, Fabrication, characterization, and acid solubility of MgO-$Nd_2Zr_2O_7$ composite ceramics for inert matrix fuel, J. Aust. Ceram. Soc. 56 (2020) 895–903.

[14] P. Anithakumari, V. Grover, C. Nandi, K. Bhattacharyya, A.K. Tyagi, Utilizing non-stoichiometry in $Nd_2Zr_2O_7$ pyrochlore: exploring superior ionic conductors, RSC Adv. 6 (2016) 97566–97579.

[15] N.V. Lyskov, A.N. Shchegolikhin, D.N. Stolbov, I.V. Kolbanev, E. Gomes, J.C. C. Abrantes, A.V. Shlyakhtina, Study of oxygen-ion conductivity and luminescence in the ZrO_2 – Nd_2O_3 system: impact of local heterogeneity, Electrochim. Acta 403 (2022), 139632.

[16] A.P. Anantharaman, H.P. Dasari, Potential of pyrochlore structure materials in solid oxide fuel cell applications, Ceram. Int. 47 (2021) 4367–4388.

[17] M. Jovaní, H. Beltrán-Mir, E. Cordoncillo, A.R. West, Field-induced p-n transition in yttria-stabilized zirconia, Sci. Rep. 9 (2019) 18538.

[18] R. Clements, J.R. Hester, B.J. Kennedy, C.D. Ling, A.P.J. Stampfl, The fluorite-pyrochlore transformation of $Ho_{2-y}Nd_yZr_2O_7$, J. Solid State Chem. 184 (2011) 2108–2113.

[19] B.P. Mandal, S.K. Deshpande, A.K. Tyagi, Ionic conductivity enhancement in $Gd_2Zr_2O_7$ pyrochlore by Nd doping, J. Mater. Res. 23 (2008) 911–916.

[20] A.V. Shlyakhtina, D.A. Belov, A.V. Knotko, M. Avdeev, I.V. Kolbanev, G. A. Vorobieva, O.K. Karyagina, L.G. Shcherbakova, Oxide ion transport in $(Nd_{2-x}Zr_x)Zr_2O_{7+\delta}$ electrolytes by an interstitial mechanism, J. Alloy. Compd. 603 (2014) 274–281.

[21] T. Hagiwara, H. Yamamura, K. Nomura, M. Igawa, Relationship between crystal structure and oxide-ion conduction in $Ln_2Zr_2O_7$ (Ln= Eu, Nd and La) system deduced by neutron and X-ray diffraction, J. Ceram. Soc. Jpn. 121 (2013) 205–210.

[22] J. Rodriguez-Carvajal, Recent advances in magnetic structure determination by neutron powder diffraction, Phys. B Condens. Matter 192 (1993) 55.

[23] I.M. Hodge, M.D. Ingram, A.R. West, Impedance and modulus spectroscopy of polycrystalline solid electrolytes, J. Electroanal. Chem. Interfacial Electrochem 74 (1976) 125–143.

[24] J.T.S. Irvine, D.C. Sinclair, A.R. West, Electroceramics: characterization by impedance spectroscopy, Adv. Mater. 2 (1990) 132–138.

[25] D.C. Sinclair, D.C. Characterization of Electro-materials using AC impedance spectroscopy, Bol. La Soc. Esp. Ceram. Y. Vidr. 65 (1995) 55–66.

[26] E.J. Abram, D.C. Sinclair, A.R. West, A strategy for analysis and modelling of impedance spectroscopy data of electroceramics: doped lanthanum gallate, J. Electroceram. 10 (2003) 165–177.

[27] X. Vendrell, A.R. West, Electrical properties of yttria-stabilized zirconia, YSZ single crystal: local AC and long range DC conduction, J. Electrochem. Soc. 165 (2018) F966–F975.

[28] C. Kaliyaperumal, A. Sankarakumar, J. Palanisamy, T. Paramasivam, Fluorite to pyrochlore phase transformation in nanocrystalline $Nd_2Zr_2O_7$, Mater. Lett. 228 (2018) 493–496.

[29] L. Kong, I. Karatchevtseva, D.J. Gregg, M.G. Blackford, R. Holmes, G. Triani, , $Gd_2Zr_2O_7$ and $Nd_2Zr_2O_7$ pyrochlore prepared by aqueous chemical synthesis, J. Eur. Ceram. Soc. 33 (2013) 3273–3285.

[30] J.L. Payne, M.G. Tucker, I.R. Evans, From fluorite to pyrochlore: characterisation of local and average structure of neodymium zirconate, $Nd_2Zr_2O_7$, J. Solid State Chem. 205 (2013) 29–34.

[31] R.D. Shannon, Revised Effective, Ionic radii and systematic studies of interatomie distances in halides and chaleogenides, Acta Crystallogr. A32 (1976) 751–767.

[32] D. Marrocchelli, S.R. Bishop, H.L. Tuller, B. Yildiz, Understanding chemical expansion in non-stoichiometric oxides: ceria and zirconia case studies, Adv. Funct. Mater. 22 (2012) 1958–1965.

[33] J. Xu, R. Xi, X. Xu, Y. Zhang, X. Feng, X. Fang, X. Wang, $A_2B_2O_7$ pyrochlore compounds: a category of potential materials for clean energy and environment protection catalysis, J. Rare Earths. 38 (2020) 840–849.

[34] M. Glerup, O.F. Nielsen, F.W. Poulsen, The structural transformation from the pyrochlore structure, $A_2B_2O_7$, to the fluorite structure, AO_2, studied by Raman spectroscopy and defect chemistry modeling, J. Solid State Chem. 160 (2001) 25–32.

[35] H.P. Chiang, B. Mou, K.P. Li, P. Chiang, D. Wang, S.J. Lin, W.S. Tse, Lattice dynamic investigation of the zone center wavenumbers of the cubic $A_2Ti_2O_7$, pyrochlores, J. Raman Spectrosc. 32 (2001) 41–44.

[36] V.G. Keramidas, W.B. White, Raman spectra of oxides with the fluorite structure, J. Chem. Phys. 59 (1973) 1561–1562.

[37] B.P. Mandal, A. Banerji, V. Sathe, S.K. Deb, A.K. Tyagi, Order-disorder transition in $Nd_{2-y}Gd_yZr_2O_7$ pyrochlore solid solution: An X-ray diffraction and Raman spectroscopic study, J. Solid State Chem. 180 (2007) 2643–2648.

[38] B.P. Mandal, P.S.R. Krishna, A.K. Tyagi, Order-disorder transition in the $Nd_{2-y}Y_yZr_2O_7$ system: probed by X-ray diffraction and Raman spectroscopy, J. Solid State Chem. 183 (2010) 41–45.

[39] C. Kaliyaperumal, A. Sankarakumar, T. Paramasivam, Grain size effect on the electrical properties of nanocrystalline $Gd_2Zr_2O_7$ ceramics, J. Alloy. Compd. 813 (2020).

[40] M.T. Vandenborre, E. Husson, J.P. Chatry, D. Michel, Rare-earth titanates and stannates of pyrochlore structure; vibrational spectra and force fields, J. Raman Spectrosc. 14 (1983) 63–71.

[41] B.P. Mandal, A. Dutta, S.K. Deshpande, R.N. Basu, A.K. Tyagi, Nanocrystalline $Nd_{2-y}Gd_yZr_2O_7$ pyrochlore: facile synthesis and electrical characterization, J. Mater. Res 24 (2009) 2855–2862.

[42] D.J. Arenas, L.V. Gasparov, W. Qiu, J.C. Nino, C.H. Patterson, D.B. Tanner, Raman study of phonon modes in bismuth pyrochlores, Phys. Rev. B - Condens. Matter Mater. Phys. 82 (2010).

[43] B.E. SCHEETZ, W.B. WHITE, Characterization of Anion Disorder in Zirconate $A_2B_2O_7$ Compounds by Raman Spectroscopy, J. Am. Ceram. Soc. 62 (1979) 468–470.

[44] Z.G. Liu, J.H. Ouyang, K.N. Sun, Y. Zhou, Electrical conductivity of 5 mol.% Yb_2O_3 and 5 mol.% Gd_2O_3 co-doped $Sm_2Zr_2O_7$, Mater. Lett. 65 (2011) 385–387.

[45] A.J. Feighery, J.T.S. Irvine, C. Zheng, High oxide ion conductivity in non-stoichiometric pyrochlores and fluorites in the ternary system ZrO_2 - Gd_2O_3 - TiO_2, Ion. (Kiel.) 3 (1997) 30–35.

[46] E.L. dos, S. Veiga, M. Fortuño-Morte, H. Beltrán-Mir, E. Cordoncillo, Effect of the oxidation states on the electrical properties of Fe-doped $Pr_2Zr_2O_7$ pyrochlore, J. Mater. Res. Technol. 16 (2022) 201–215.

[47] C.-K. Hao, H.-E. Hung, C.-S. Lee, Characterization and electrochemical properties of chromium-substituted pyrochlore $Y_2Ti_{2-x}Cr_xO_{7-\delta}$, J. Sol. -Gel Sci. Technol. 76 (2015) 428–435.

[48] R. Martínez-Coronado, J.A. Alonso, M.T. Fernández, Synthesis and characterization of R_2MnTiO_7 (R=Y and Er) pyrochlores oxides, Mater. Res. Bull. 48 (2013) 3304–3309.

[49] D.M. Smyth, The Defect Chemistry of Metal Oxides, Oxford University Press, 2000.

[50] X. Vendrell, A.R. West, Induced p- type semiconductivity in yttria-stabilized zirconia, J. Am. Ceram. Soc. 102 (2019) 6100–6106.

[51] M. Jovaní, H. Beltrán-Mir, E. Cordoncillo, A.R. West, Atmosphere- and voltage-dependent electronic conductivity of oxide-ion-conducting $Zr_{1-x}Y_xO_{2-x/2}$ Ceramics, Inorg. Chem. 56 (2017) 7081–7088.

[52] N. Masó, A.R. West, Electronic conductivity in yttria-stabilized zirconia under a small dc bias, Chem. Mater. 27 (2015) 1552–1558.

[53] N. Masó, M. Prades, H. Beltrán, E. Cordoncillo, D.C. Sinclair, A.R. West, Field enhanced bulk conductivity of acceptor-doped $BaTi_{1-x}Ca_xO_{3-x}$ ceramics, Appl. Phys. Lett. 97 (2010).

[54] M. Prades, N. Masó, H. Beltrán, E. Cordoncillo, A.R. West, Field enhanced bulk conductivity of $BaTiO_3$:Mg ceramics, J. Mater. Chem. 20 (2010) 5335.